Chapter 9 in the book:
P.A. Kralchevsky and K. Nagayama, "Particles at Fluid Interfaces and Membranes"
(Attachment of Colloid Particles and Proteins to Interfaces and Formation of Two-Dimensional Arrays)
Elsevier, Amsterdam, 2001; pp. 396-425.

CHAPTER 9

CAPILLARY FORCES BETWEEN PARTICLES BOUND TO A SPHERICAL INTERFACE

This chapter contains theoretical results about the lateral capillary interaction between two particles bound to a spherical fluid interface, liquid film, lipid vesicle or membrane. The capillary forces in this case can be only of "immersion" type. The origin of the interfacial deformation and capillary force can be the entrapment of the particles in the liquid film between two phase boundaries, or the presence of applied stresses due to outer bodies. The stability of a liquid film is provided by a repulsive disjoining pressure, which determines the capillary length q^{-1} and the range of the particle-particle interaction. The calculation of the capillary force is affected by the specificity of the spherical geometry. The spherical bipolar coordinates represent the natural set of coordinates for the mathematical description of the considered system. They reduce the integration domain to a rectangle and make easier the numerical solution of the Laplace equation. Two types of boundary conditions, fixed contact angle and fixed contact line, can be applied. Coupled with the spherical geometry of the interface they lead to qualitatively different dependencies of the capillary force on distance. The magnitude of the capillary interaction energy can be again of the order of 10–100 kT for small sub-micrometer particles. In such a case, the capillary attraction prevails over the thermal motion and can bring about particle aggregation and ordering in the spherical film. In this respect, the physical situation is the same for spherical and planar films, if only the particles are subjected to the action of the lateral immersion force. The study of a film with one deformable surface, described in this chapter, is the first step toward the investigation of more complicated systems with two deformable surfaces such as a spherical emulsion film or a spherical lipid vesicle containing inclusions.

9.1. ORIGIN OF THE "CAPILLARY CHARGE" IN THE CASE OF SPHERICAL INTERFACE

Spherical interfaces and membranes can be observed frequently in nature, especially in various emulsion and biological systems [1-3]. As a rule, the droplets in an emulsion are polydisperse in size, and consequently, the liquid films intervening between two attached emulsion drops have in general spherical shape [4]. It is worthwhile noting that some emulsions exist in the form of globular liquid films, which can be of W1/O/W2 or O1/W/O2 type (O = oil, W = water), see e.g. Ref. [5]. If small colloidal particles are bound to such spherical interfaces (thin films, liposomes, membranes, etc.) they may experience the action of lateral capillary forces.

The spherical geometry provides some specific conditions, which differ from those with planar interfaces or plane-parallel thin films. For example, in the case of closed spherical thin film it is important that the volume of the liquid layer is finite. In addition, the capillary force between two diametrically opposed particles, confined in a spherical film, is zero irrespective of the range of the interaction determined by the characteristic capillary length q^{-1}.

As already discussed, the particles attached to an interface (thin film, membrane) interact through the overlap of the perturbations in the interfacial shape created by them. This is true also when the non-disturbed interface is spherical; in this case any deviation from the spherical shape has to be considered as an interfacial perturbation, which gives rise to the particle "capillary charge", see Section 7.1.3 above. The effect of gravity is negligible in the case of spherical interfaces (otherwise the latter will be deformed), and consequently, it is not expected the particle weight to cause any significant interfacial deformation. Then a question arises: which can be the origin of the interfacial perturbations in this case?

Let us consider an example depicted in Fig. 9.1a: a solid spherical particle attached to the surface of a spherical emulsion drop of radius R_0. Such a configuration is typical for the Pickering emulsions which are stabilized by the adsorption of solid particles and have a considerable importance for the practice [6-10]. The depth of immersion of the particle into the drop phase, and the radius of the three-phase contact line, r_c, is determined by the value of the contact angle α (Fig. 9.1a). The pressure within the drop, P_1, is larger than the outside pressure

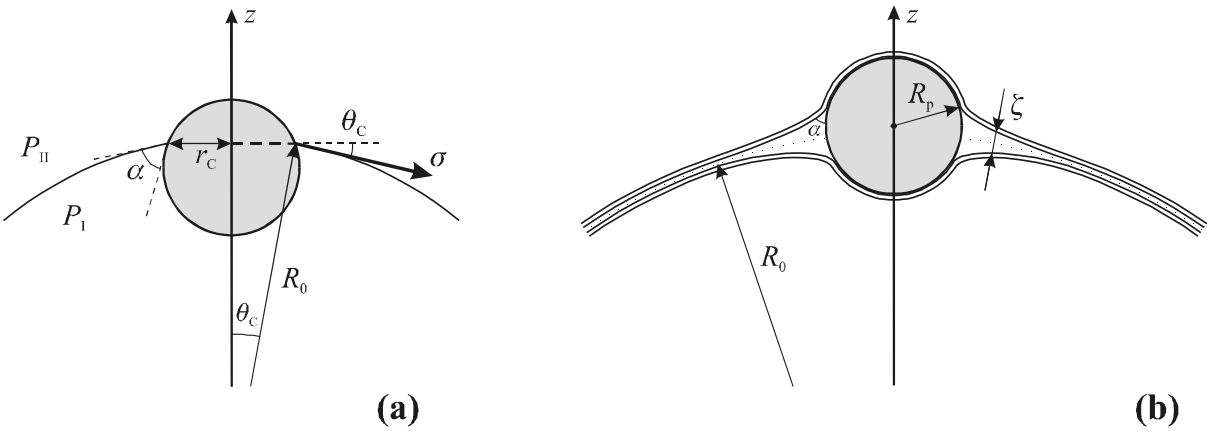

Fig. 9.1. (a) Spherical particle attached to the surface of an emulsion drop of radius R_0; α is the three phase contact angle; r_c is the contact line radius; P_I and P_{II} are the pressures inside and outside the drop. (b) Particle of radius R_p entrapped between the two lipid bilayers composing a spherical vesicle of radius R_0; ζ is the running thickness of the gap (filled with water) between the two detached bilayers.

P_{II} because of the curvature of the drop surface. The force pushing the particle outside the drop (along the z-axis) is

$$F_{out} = \pi r_c^2 P_I ; \tag{9.1}$$

on the other hand, the force pushing the particle inside the drop is due to the outer pressure and the drop surface tension resolved along the z-axis (Fig. 9.1a):

$$F_{in} = \pi r_c^2 P_{II} + 2\pi r_c \sigma \sin\theta_c \quad . \tag{9.2}$$

Here θ_c is a central angle: $\sin\theta_c = r_c/R_0$. At equilibrium one must have $F_{in} = F_{out}$; then combining Eqs. (9.1) and (9.2) one obtains the Laplace equation $P_I - P_{II} = 2\sigma/R_0$ which is identically satisfied for a spherical interface. Thus we arrive at the conclusion that the force balance $F_{in} = F_{out}$ is fulfilled for a spherical interface.

The same conclusion can be reached in a different way. The configuration of a spherical particle attached to an emulsion drop must have rotational symmetry. It is known [11] that for an axisymmetric surface intersecting the axis of revolution the Laplace equation, Eq. (2.24), has a single solution: sphere (gravity deformation negligible). If a second particle is attached to the drop surface it can acquire the same configuration as that in Fig. 9.1a; only the radius of the spherical surface will slightly increase due two the volume of the drop phase displaced by the

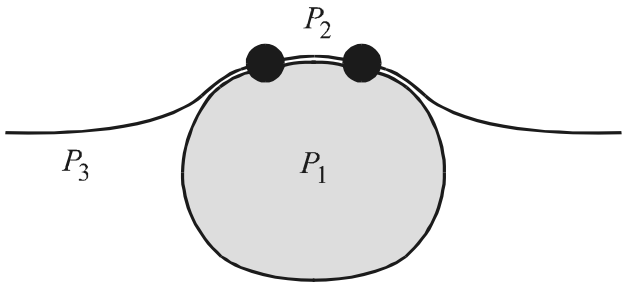

Fig. 9.2. Sketch of two solid particles entrapped into a spherical film which intervenes between two emulsion drops of different size; P_1 and P_2 denote the pressures into the two drops and P_3 is the pressure in the continuous phase.

second particle. In other words the force balance $F_{in} = F_{out}$ is fulfilled for each separate particle and the drop surface remains spherical. Moreover, if there is no deviation from the spherical shape, then lateral capillary force between the particles *cannot* appear. Hence, if aggregation of particles attached to the surface of such emulsion drop is observed, it should be attributed to other kind of forces.

After the last 'negative' example, let us consider another example, in which both deformation and lateral capillary forces do appear. Pouligny and co-authors [12-14] have studied the sequence of phenomena which occur when a solid latex microsphere is brought in contact with an isolated giant spherical phospholipid vesicle. They observed a spontaneous attachment (adhesion) of latex particles to the vesicle, which is accompanied by complete or partial wetting (wrapping) of the particle by lipid bilayer(s). In fact, the membrane of such a vesicle can be composed of two or more lipid bilayers. As an example, in Fig. 9.1b we present a configuration of a membrane consisting of two lipid bilayers; the particle is captured between the two bilayers. The observations show that such two captured particles experience a long range attractive force [15]. There are experimental indications that in a vicinity of the particle the two lipid bilayers are detached (Fig. 9.1b) and a gap filled with water is formed between them [15]. The latter configuration resembles that depicted in Fig. 7.1f, and consequently, the observed long range attraction could be attributed to the capillary immersion force [15]. Similar configurations can appear also around particles, which are confined in the spherical film intervening between two attached emulsion droplets (Fig. 9.2), or in the globular emulsion films like those studied in Ref. [5]. In these cases the interfacial deformations are related to the confinement of the particles within the film.

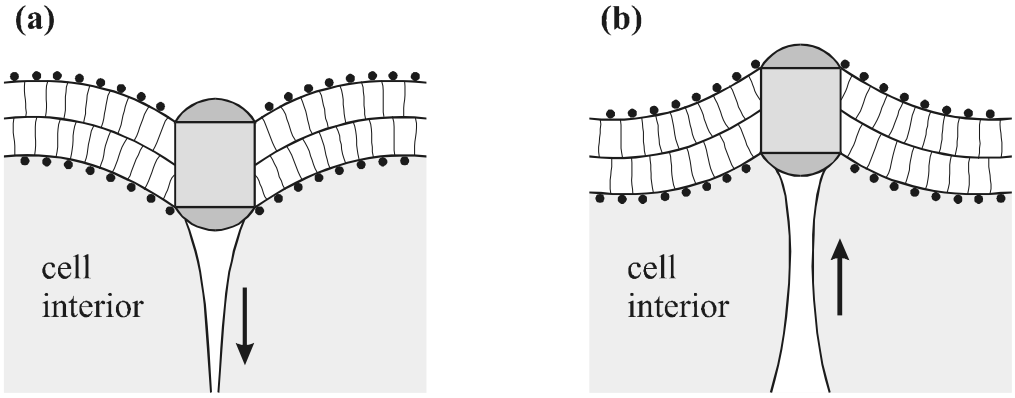

Fig. 9.3. Deformations in the membrane of a living cell due to (a) a microfilament pulling an inclusion inward and (b) a microtubule pushing an inclusion outward.

Looking for an example in biology, we could note that the cytoskeleton of a living cell is a framework composed of interconnected microtubules and filaments, which resembles a "tensegrity" architectural system composed of long struts joined with cables, see Refs. [16,17]. Moreover, inside the cell a gossamer network of contractile microfilaments pulls the cell's membrane toward the nucleus in the core [17]. In the points where the microfilaments are attached to the membrane, concave "dimples" will be formed, see Fig. 9.3a. On the other hand, at the points where microtubules (the "struts") touch the membrane, the latter will acquire a "pimple"-like shape, see Fig. 9.3b. Being deformations in the cell membrane, these "dimples" and "pimples" will experience lateral capillary forces, both attractive and repulsive, which can be employed to create a more adequate mechanical model of a living cell and, hopefully, to explain the regular "geodesic forms" which appear in some biological structures [17].

Other example can be a lipid bilayer (vesicle) containing incorporated membrane proteins, around which some local variation in the bilayer thickness can be created. The latter is due to the mismatch in the thickness of the hydrophobic zones of the protein and the bilayer. The overlap of such deformations can give rise to a membrane-mediated protein-protein interaction [18]. A peculiarity of this system, which is considered in Chapter 10 below, is that the hydrocarbon core of the lipid bilayer exhibits some elastic properties and cannot be treated as a simple fluid [19,20].

Coming back to simpler systems, in which lateral capillary forces can be operative, we should mention a configuration of two particles (Fig. 9.4b), which are confined in a liquid film wetting a bigger spherical *solid* particle. The problem about the capillary forces experienced by such two particles has been solved in Ref. [21]. The developed theoretical approach, which is applicable (with possible modifications) also to the other systems mentioned above, is described in the rest of the present chapter.

9.2. INTERFACIAL SHAPE AROUND INCLUSIONS IN A SPHERICAL FILM

9.2.1. LINEARIZATION OF LAPLACE EQUATION FOR SMALL DEVIATIONS FROM SPHERICAL SHAPE

Figure 9.4 shows schematically a spherical solid substrate (I) of radius R_s covered with a liquid film (F) intervening between the substrate and the outer fluid phase (II). The film contains two identical entrapped particles which deform the outer film surface. The non-disturbed spherical liquid film can have a stable equilibrium thickness h_0 only due to the action of some repulsive forces (positive disjoining pressure) between the two film surfaces. For that reason a *thin* film,

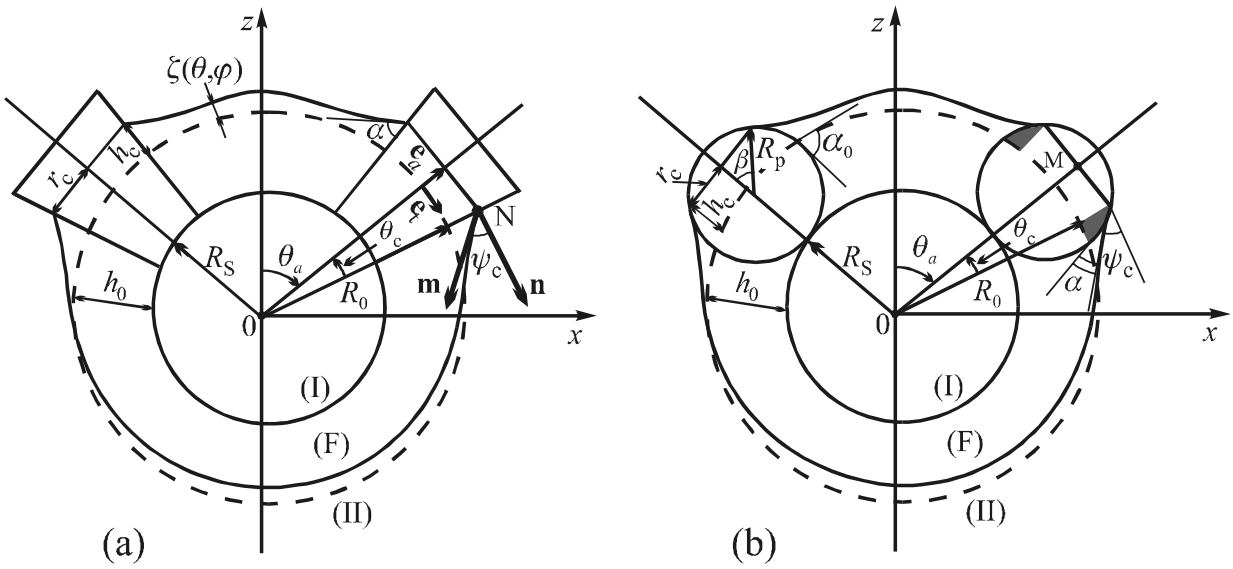

Fig. 9.4. (a) Two 'cork-shaped' particles and (b) two spherical particles of radius R_p protruding from a liquid layer on a solid substrate of radius R_s ; the angles θ_a and θ_c characterize the particle positions and size; r_c is the contact line radius; h_c is the elevation of the contact line above the level of the reference sphere of radius R_0; α is the three-phase contact angle; in both (a) and (b) the meniscus slope angle ψ_c is subtended between the normal to the segment ON and the tangent to the meniscus [21].

i.e. a film for which the effect of the disjoining pressure Π is not negligible, is considered here. Below we restrict our considerations to film thickness and particle size much smaller than R_s.

An auxiliary system is depicted in Fig. 9.4a, in which each of the two particles have the special shape of a part of slender cone with vertex in the center of the substrate. In Ref. [21] it has been demonstrated, that the consideration of such *cork-shaped* particles is useful for the subsequent treatment of the more realistic system with two *spherical* particles depicted in Fig. 9.4b. We will first present the results for cork-shaped particles, which will be further extended to spherical particles in Section 9.3.3 below.

The deviation of the outer film surface (Fig. 9.4) from the spherical shape is caused by the capillary rise of the liquid along the particle surface to form an equilibrium three-phase contact angle α. For given radius of the substrate, film volume and particle shape there is one special value α_0 of the contact angle (Fig. 9.4b), which corresponds to spherical shape of the outer film surface ($\alpha_0 = \pi/2$ for the configuration in Fig. 9.4a). The radius of this sphere is denoted by R_0; below it will be termed the *reference sphere* [21] and the interfacial deformations created by the trapped particles (for $\alpha \neq \alpha_0$) will be accounted with respect to this spherical surface.

The radial coordinate of a point of the deformed film surface can be presented in the form

$$r = R_0 + \zeta(\theta,\varphi) \tag{9.3}$$

where θ and φ are standard polar and azimuthal angles on the reference sphere $r = R_0$ and $\zeta(\theta,\varphi)$ expresses the interfacial deformation due to the presence of the two particles. We assume small deformations,

$$|\zeta/R_0| << 1 \qquad \text{and} \qquad |\nabla_{\text{II}}\zeta|^2 << 1, \tag{9.4}$$

where ∇_{II} denotes surface gradient operator in the reference sphere. At static conditions the interfacial shape obeys the Laplace equation of capillarity, which in view of Eq. (9.4) can be linearized [22,23]:

$$P_R + \Pi(h) - P_{\text{II}} = \sigma(h)\left(\frac{2}{R_0} - \frac{2\zeta}{R_0^2} - \nabla_{\text{II}}^2\zeta\right) \tag{9.5}$$

Here P_{II} is the pressure in the outer fluid (II), P_R is the reference pressure in the thin liquid film, Π is disjoining pressure and σ is the interfacial tension of the boundary film–phase II. If the liquid film contacts with a bulk liquid phase, as it is in Fig. 9.2, then the reference pressure can be identified with the pressure in this phase, that is $P_R = P_3$ for the system depicted in Fig. 9.2. On the other hand, if the film is closed as it is in Fig. 9.4, then P_R can be determined from the condition for constancy of the volume of this film, see Eq. (9.18) below. For $\zeta \to 0$ Eq. (9.5) reduces to the Laplace equation for the surface of a spherical thin liquid film, see Eqs. (6.8)-(6.10) and Ref. [24].

Both Π and σ depend on the film thickness

$$h = h_0 + \zeta, \qquad h_0 \equiv R_0 - R_s = \text{const.} \tag{9.6}$$

Moreover, for a wetting film Π and σ are connected by means of the relationship [25]

$$\sigma(h) = \sigma_\infty + \int_h^\infty \Pi(h)\, dh, \tag{9.7}$$

where σ_∞ is the surface tension of the bulk liquid phase (infinitely thick film), see Eq. (5.8) above. The integral term in Eq. (9.7) expresses the equilibrium work (per unit area) carried out by the surface forces to bring the two film surfaces from infinity to a finite separation h. For $\zeta << h_0$, using Eqs. (9.6) and (9.7), one can expand $\Pi(h)$ and $\sigma(h)$ in series:

$$\Pi = \Pi_0 + \Pi' \zeta + ..., \qquad \sigma = \sigma_0 - \Pi_0 \zeta - \tfrac{1}{2} \Pi' \zeta^2 + ..., \tag{9.8}$$

where

$$\sigma_0 = \sigma\big|_{h=h_0}, \qquad \Pi_0 = \Pi\big|_{h=h_0}, \qquad \Pi' = (\mathrm{d}\Pi/\mathrm{d}h)\big|_{h=h_0}, \tag{9.9}$$

Next, we substitute Eq. (9.9) into Eq. (9.5) and obtain the linearized Laplace equation in the form [21]

$$\nabla_{II}^2 \zeta - q^2 \zeta = 2\Delta H, \tag{9.10}$$

where the following notation has been introduced:

$$q^2 \equiv -\frac{\Pi'}{\sigma_0} - \frac{2}{R_0} - \frac{2\Pi_0}{\sigma_0 R_0} \tag{9.11}$$

$$\Delta H \equiv \frac{1}{R_0} - \frac{1}{R}, \qquad \frac{1}{R} \equiv \frac{1}{2\sigma_0}(P_R + \Pi_0 - P_{II}) \tag{9.12}$$

Here q^{-1} has the meaning of capillary length, which determines the range of the interfacial deformation and of the lateral capillary force; note that for $R_0 \to \infty$ Eq. (9.11) reduces to the form of Eq. (7.7) for flat thin films. On the other hand, if disjoining pressure is missing (as it is for the systems depicted in Fig. 9.3) then $q^2 = -2/R_0$; in such a case q will be an imaginary number and the Laplace equation, Eq. (9.10), will have oscillatory solutions. Following Ref. [21], we will assume that the effect of disjoining pressure is predominant (this guarantees the stability of the films in Figs. 9.2 or 9.4), and we work with real values of the parameter q. Indeed, for stable films $\Pi' < 0$, see e.g. Ref. [26]; we assume that $|\Pi'|$ is large enough to have $q^2 > 0$.

In Eq. (9.12) ΔH stands for the change in the mean curvature of the film surface due to the deformation caused by the two entrapped particles (Fig. 9.4); R can be interpreted as the outer radius of an imaginary spherical layer of thickness h_0, whose internal pressure is equal to the pressure inside the perturbed film [21].

9.2.2. "CAPILLARY CHARGE" AND REFERENCE PRESSURE

ΔH and P_R can be determined from the physical condition that the volume of the liquid film does not change, i.e. the liquid within the film is incompressible and the phase boundaries are closed for the exchange of molecules with the neighboring phases [21]. In such a case the integral

$$V_m \equiv \iint_{S_0} d\theta\, d\varphi \sin\theta \int_{R_0}^{R_0+\zeta} dr r^2 = \int_{S_0} ds \left(\zeta + \frac{\zeta^2}{R_0} + \frac{\zeta^3}{3R_0^2} \right), \tag{9.13}$$

expressing the change in the film volume due to the surface deformation, must be equal to zero; the integration is taken over the surface domain S_0 representing the radial projection of the deformed film surface on the reference sphere; ds is a surface element. For the system with cork-shaped particles (Fig. 9.4a) $V_m = 0$ is a rigorous relationship, whereas for the system with

spherical particles $V_m = 0$ is an approximate expression because the small volumes shown shaded in Fig. 9.4b are neglected. Linearizing the integrand in Eq. (9.13) and substituting ζ from Eq. (9.10) one derives [21]

$$0 = V_m \approx \int_{S_0} ds\zeta = q^{-2} \int_{S_0} ds(\nabla_{\mathrm{II}}^2 \zeta - 2\Delta H) \tag{9.14}$$

Further, from Eq. (9.14) one obtains

$$8\pi R_0^2 \Delta H \approx \int_{S_0} ds 2\Delta H = \int_{S_0} ds \nabla_{\mathrm{II}} \cdot (\nabla_{\mathrm{II}} \zeta) = \sum_{k=1}^{2} \oint_{C_k} dl \tilde{\mathbf{n}} \cdot \nabla_{\mathrm{II}} \zeta , \qquad (r_0/R_0)^2 << 1 \tag{9.15}$$

At the last step we have used the Green-Gauss-Ostrogradsky theorem, see e.g. Refs. [27-29]; C_k (k = 1,2) are two circular contours representing the orthogonal (radial) projections of the two particle contact lines onto the reference sphere of radius R_0; dl is a linear element; $\tilde{\mathbf{n}}$ is a unit running normal to C_k directed inwards. The linear integral yields

$$\oint_{C_k} dl \tilde{\mathbf{n}} \cdot \nabla_{\mathrm{II}} \zeta = 2\pi r_0 \tan\psi_c , \qquad r_0 \equiv R_0 \sin\theta_c \tag{9.16}$$

where $\tan\psi_c$ is the average meniscus slope at the contact line, see Fig. 9.4, and r_0 is the radius of the circumference C_k. In the case of fixed contact angle α, for the system depicted in Fig. 9.4a $\psi_c = \pi/2 - \alpha$ = const. and one can directly write $\tilde{\mathbf{n}} \cdot \nabla_{\mathrm{II}} \zeta = \tan\psi_c$. Finally, combining Eqs. (9.15) and (9.16) one obtains the sought-for expression for ΔH [21]:

$$\Delta H \approx Q/(2R_0^2), \qquad Q \equiv r_0 \sin\psi_c \approx r_0 \tan\psi_c \qquad (\sin^2\psi_c << 1) \tag{9.17}$$

Here, as usual, Q denotes the "capillary charge" of the entrapped particles, cf. Eqs. (7.9) and (7.14). Finally, from Eqs. (9.12) and (9.17) one determines the reference pressure inside the closed film [21]:

$$P_R = P_{\mathrm{II}} - \Pi_0 + 2\sigma_0/R_0 - \sigma_0 Q/R_0^2 \tag{9.18}$$

Since ΔH is constant (independent of the surface coordinates θ and φ) it is convenient to present Eq. (9.10) in the simpler form

$$\nabla_{\mathrm{II}}^2 \tilde{\zeta} = q^2 \tilde{\zeta} , \tag{9.19}$$

where

$$\tilde{\zeta} \equiv (\zeta + 2q^{-2}\Delta H)/R_0 \tag{9.20}$$

9.2.3. INTRODUCTION OF SPHERICAL BIPOLAR COORDINATES

To integrate conveniently Eq. (9.19) special bipolar coordinates on a sphere have been invented in Ref. [21]. The connection between the Cartesian coordinates (x,y,z) and these curvilinear coordinates (r,ω,τ) are:

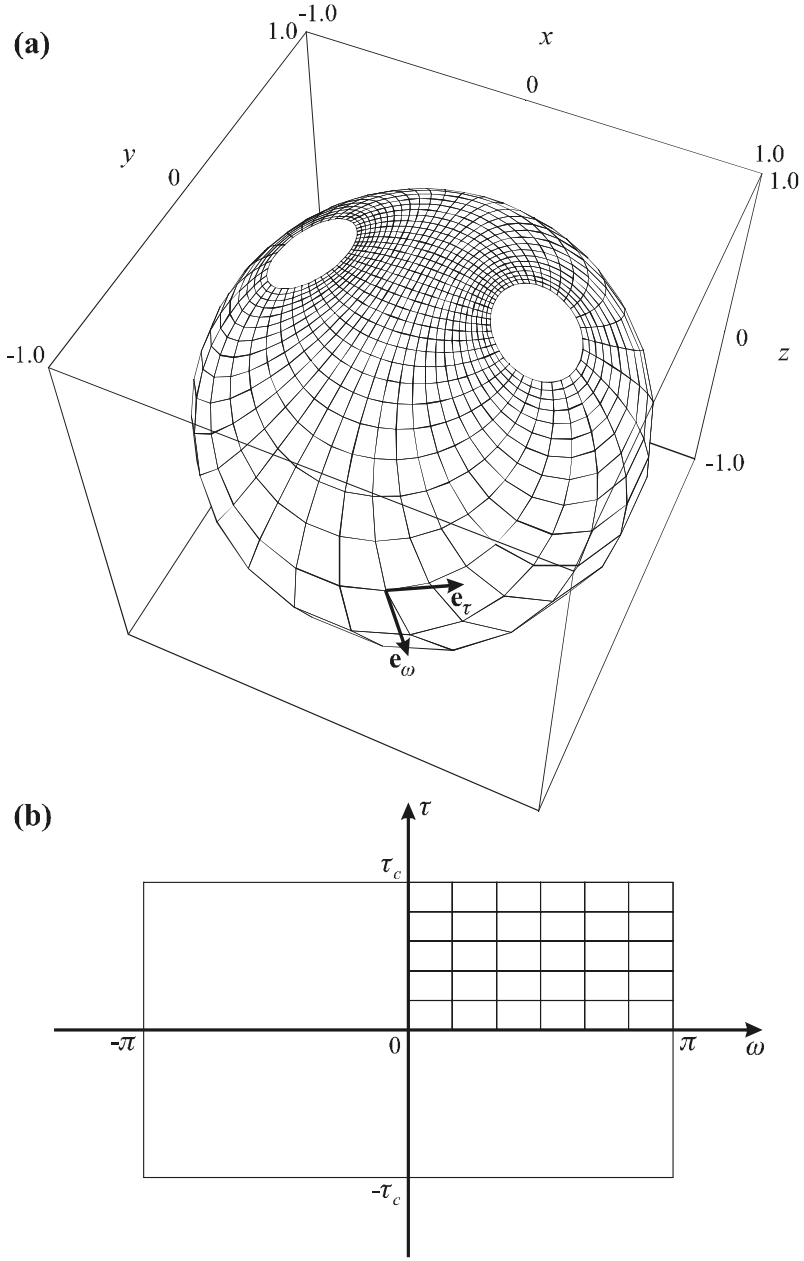

Fig. 9.5. (a) Bipolar coordinate lines on the unit sphere: the lines τ = const. are analogous to the parallels, while the lines ω = const. connecting the two "poles" resemble meridians, cf. Eq. (9.21). (b) The parametrization of the reference sphere, $r = R_0$ in Fig. 9.4, by means of spherical bipolar coordinates reduces the integration domain of Eq. (9.19) to a rectangle; after Ref. [21].

$$x = \frac{r\sqrt{\lambda^2 - 1}\sinh\tau}{\lambda\cosh\tau - \cos\omega}, \qquad y = \frac{r\sqrt{\lambda^2 - 1}\sin\omega}{\lambda\cosh\tau - \cos\omega}, \qquad z = \frac{r(\cosh\tau - \lambda\cos\omega)}{\lambda\cosh\tau - \cos\omega} \tag{9.21}$$

The surfaces r = const. are spheres; the lines ω = const. (on each sphere r = const.) are circumferences which are counterparts of the meridians; the lines τ = const. are circumferences – counterparts of the parallels of latitude, see Fig. 9.5a. In each point on the sphere the respective τ-line and ω-line are orthogonal to each other. These bipolar coordinates on a sphere induce orthogonal biconical coordinates in space, which in fact are defined by Eq. (9.21). A detailed description of these coordinates can be found in Ref. [21], including expressions for the components of the metric tensor and Christoffel symbols, for various differential operators, components of the rate-of-strain tensor and the respective form of the Navier-Stokes equation.

In the special case considered here we will use the spherical bipolar coordinates (ω, τ) for a parametrization of the reference sphere $r = R_0$ = const. In terms of these coordinates the surface gradient operator acquires the form [21]

$$\nabla_{\mathrm{II}}\zeta = \frac{1}{\chi}\left(\mathbf{e}_\omega\frac{\partial\zeta}{\partial\omega} + \mathbf{e}_\tau\frac{\partial\zeta}{\partial\tau}\right) \tag{9.22}$$

where

$$\chi \equiv \frac{a}{\lambda\cosh\tau - \cos\omega}, \qquad a \equiv R_0(\lambda^2 - 1)^{1/2} \tag{9.23}$$

$\mathbf{e}_\omega$ and $\mathbf{e}_\tau$ are the unit vectors of the local surface basis. With the help of the spherical bipolar coordinates we bring Eq. (9.19) in the form [21]

$$(\lambda\cosh\tau - \cos\omega)^2\left(\frac{\partial^2\tilde{\zeta}}{\partial\omega^2} + \frac{\partial^2\tilde{\zeta}}{\partial\tau^2}\right) = (qa)^2\tilde{\zeta}(\omega,\tau) \tag{9.24}$$

where a is defined by Eq. (9.23); note that Eq. (9.24) much resembles Eq. (7.32). The parameter λ, which depends on the distance between the two particles, is defined by means of the expression [21]

$$\lambda = \frac{\cos\theta_c}{\cos\theta_a} \qquad (\theta_a \geq \theta_c) \tag{9.25}$$

Note that λ can vary in the interval $1 \le \lambda \le \infty$; in particular, $\lambda = 1$ when the two particles in Fig. 9.4a touch each other, while $\lambda = \infty$ when the particles are diametrically opposed. The contact lines on the two particles correspond to $\tau = \pm\tau_c$, where [21]:

$$\tau_c \equiv \operatorname{arctanh}[(\cos^2\theta_c - \cos^2\theta_a)^{1/2}/\sin\theta_a] \qquad (\theta_c \le \theta_a \le \pi/2) \tag{9.26}$$

Thus the integration domain of Eq. (9.24) acquires the simple form of a rectangle, see Fig. 9.5b:

$$-\pi \le \omega \le +\pi, \qquad -\tau_c \le \tau \le +\tau_c \tag{9.27}$$

The boundary condition of fixed contact angle (stemming from the Young equation) for the system depicted in Fig. 9.4a implies

$$\tilde{\mathbf{n}}\cdot\nabla_{II}\zeta = (-1)^k \tan\psi_c \qquad \text{at contour } C_k \qquad (k = 1, 2) \tag{9.28}$$

$\tilde{\mathbf{n}}$ has the same meaning as in Eq. (9.15); since C_k represents a line of fixed τ-coordinate ($\tau = \pm\tau_c$), then $\tilde{\mathbf{n}} = \pm\mathbf{e}_\tau$ at the contour C_k. Thus with the help of Eqs. (9.20), (9.22) and (9.23) the boundary condition (9.28) can be expressed in the form [21]

$$\left(\frac{\partial\tilde{\zeta}}{\partial\tau}\right)_{\tau=\tau_c} = \frac{\sin\psi_c\sqrt{\lambda^2-1}}{\lambda\cosh\tau_c - \cos\omega} \qquad \text{(fixed contact angle)} \tag{9.29}$$

The boundary condition of fixed contact line has the same physical meaning as in Sections 7.3.4 and 8.2.1: the position of the contact line is fixed at some edge on the particle surface or at the boundary between hydrophilic and hydrophobic domains. In this case $\zeta = h_c$ = const. at the contact line, see Fig. 9.4. The linear elements along the ω-lines and τ-lines in spherical bipolar coordinates are

$$dl_\omega = \chi d\omega, \qquad dl_\tau = \chi d\tau \tag{9.30}$$

Taking into account Eqs. (9.16), (9.17), (9.20), (9.22) and (9.30), the boundary condition $\zeta = h_c$ can be expressed in terms of $\tilde{\zeta}$ [21]:

$$\tilde{\zeta}\Big|_{\tau=\tau_c} = \frac{h_c}{R_0} + \frac{1}{\pi q^2 R_0^2}\int_0^\pi d\omega\left(\frac{\partial\tilde{\zeta}}{\partial\tau}\right)_{\tau=\tau_c} \qquad \text{(fixed contact line)} \tag{9.31}$$

Note that when the position of the contact line is fixed on the surface of an axisymmetric particle, the exact shape of the particle (cork-like or spherical) is not important insofar as in all cases the contact line is a circumference of a given fixed radius. In this aspect Eq. (9.31) is applicable for both types of particles depicted in Fig. 9.4.

9.2.4. PROCEDURE OF CALCULATION AND NUMERICAL RESULTS

To obtain numerical results about the interfacial shape, and further to apply them to the calculation of the lateral capillary force (Section 9.3 below), we first have to specify the input parameters. It is convenient to scale all parameters using the reference radius R_0 and the interfacial tension σ_0; then in the computations one can work only in terms of dimensionless parameters and variables. Thus the input parameters characterizing the film are h_0/R_0 and qR_0. The input parameters related to the confined particles are θ_a, θ_c and h_c/R_0 (or α) when the contact line (or the contact angle) on the particle is fixed. Next, λ and τ_c are calculated by means of Eqs. (9.25) and (9.26). In the considered case of spherical geometry the distance between the two particles can be characterized by the length of the shortest arc connecting the axes of the two particles: $L = 2\theta_a R_0$. In the numerical calculations it is convenient to use the dimensionless distance

$$\widetilde{L} \equiv L/(\pi R_0) = 2\theta_a/\pi \qquad (2\theta_c/\pi \le \widetilde{L} \le 1) \tag{9.32}$$

Note that the maximum value $\widetilde{L} = 1$ corresponds to a configuration of two diametrically opposed particles.

As already mentioned, the usage of spherical bipolar coordinates transforms the domain of integration of Eq. (9.24) into a rectangle in the (ω,τ)-plane, which is bounded by the lines $\omega = \pm\pi$ and $\tau = \pm\tau_c$, see Fig. 9.5b. Due to the symmetry it is enough to find the meniscus profile $\widetilde{\zeta}(\omega,\tau)$ only in a quarter of this rectangle, say in the quadrant $0 \le \omega \le \pi$, $0 \le \tau \le \tau_c$. The symmetry implies the following additional boundary conditions at the inner boundaries of the quadrant:

$$\left(\frac{\partial\widetilde{\zeta}}{\partial\omega}\right)_{\omega=0} = \left(\frac{\partial\widetilde{\zeta}}{\partial\omega}\right)_{\omega=\pi} = 0, \qquad \left(\frac{\partial\widetilde{\zeta}}{\partial\tau}\right)_{\tau=0} = 0 \tag{9.33}$$

The rectangular shape of the integration domain considerably simplifies and accelerates the numerical solution of Eq. (9.24) obeying the boundary conditions (9.29) and (9.33), or alternatively, (9.31) and (9.33). In Ref. [21] the conventional finite difference scheme of second order was used for discretization of the boundary problem. In this way for each node of the integration network one linear algebraic equation was obtained. The resulting set of equations was solved by means of the Gauss-Seidel iterative method [30,31] combined with successive over-relaxation (SOR) and the Chebyshev acceleration technique [32].

When the boundary condition for *fixed contact line*, Eq. (9.31), is used, the numerical procedure can be simplified if one seeks a solution in the form [21]

$$\widetilde{\zeta}\,(\omega,\tau) = A\, f(\omega,\tau), \qquad A = \text{const.} \tag{9.34}$$

The constant A is determined as follows. The function $f(\omega,\tau)$ apparently satisfies Eq. (9.24) and the boundary conditions (9.33) with f instead of $\widetilde{\zeta}$. Then one imposes the requirement

$$\widetilde{\zeta}\Big|_{\tau=\tau_c} = A \quad \text{or} \quad f\Big|_{\tau=\tau_c} = 1 \qquad \text{(fixed contact line)} \tag{9.35}$$

Combining Eqs. (9.31) and (9.35) one determines the constant A :

$$A = \frac{h_c}{R_0}\left[1 - \frac{1}{\pi q^2 R_0^2}\int_0^{\pi} d\omega \left(\frac{\partial f}{\partial \tau}\right)_{\tau=\tau_c}\right]^{-1} \tag{9.36}$$

One has to first solve (numerically) the boundary problem for $f(\omega,\tau)$, then to calculate A from Eq. (9.36) and finally to determine $\widetilde{\zeta}(\omega,\tau)$ from Eq. (9.34).

When the boundary condition for *fixed contact angle*, Eq. (9.29), is used, the average elevation of the contact line, h_c, is not constant, but varies with the distance L between the two particles. From the calculated meniscus shape one can determine h_c by means of the equation [21]

$$\widetilde{h}_c \equiv \frac{h_c}{R_0} \equiv \oint_{C_k} \zeta_c\, dl = \frac{\sqrt{\lambda^2-1}}{\pi \sin\theta_c}\int_0^{\pi} \frac{\widetilde{\zeta}(\omega,\tau_c)\, d\omega}{\lambda\cosh\tau_c - \cos\omega} - \frac{\sin\psi_c \sin\theta_c}{q^2 R_0^2} \tag{9.37}$$

where $\zeta_c(\omega)$ expresses the position of the contact line on the particle surface:

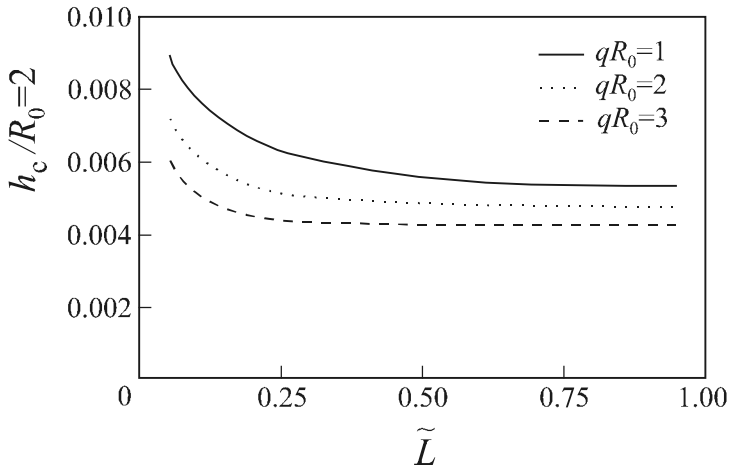

Fig. 9.6. Plot of the dimensionless average capillary elevation, h_c/R_0, vs. the dimensionless distance $\tilde{L}$ between two "cork-shaped" particles (Fig. 9.4a) calculated in Ref. [21] for three different values of the parameter qR_0 at fixed values of the angles $\theta_c = 2°$ and $\psi_c = 3°$.

$$\zeta_c(\omega) \equiv \zeta(\omega, \tau_c) \tag{9.38}$$

As an illustrative example in Fig. 9.6 we show the dependence of the dimensionless elevation $\tilde{h}_c$ on the dimensionless interparticle distance $\tilde{L}$ for three different values of qR_0 for cork-shaped particles (Fig. 9.4a). The values of the other parameters, $\theta_c = 2°$ and $\psi_c = 3°$, are the same for the three curves in Fig. 9.6. The increase of $\tilde{h}_c$ with the decrease of $\tilde{L}$ is due to the increasing overlap of the menisci created by the two particles. Since q^{-1} is the characteristic size (length) of the meniscus zone, at fixed $\tilde{L}$ the overlap is greater (and consequently h_c is larger) when q^{-1} is greater, i.e. qR_0 is smaller, see Fig. 9.6.

The overlap of the menisci around the two particles has also another consequence: in general the contact line is inclined, i.e. it does not lie in a plane perpendicular to the particle axis. This effect is similar to that with the two vertical cylinders in Fig. 7.10. For small particles ($r_c << R_0$) this inclination turns out to be very small. Indeed, it can be characterized by the angle η_c defined as follows [21]

$$\tan\eta_c \equiv \frac{\zeta_c(\pi) - \zeta_c(0)}{2r_c} = \frac{\tilde{\zeta}_c(\pi) - \tilde{\zeta}_c(0)}{2(1+\tilde{h}_c)\sin\theta_c} \qquad r_c = (R_0 + h_c)\sin\theta_c \tag{9.39}$$

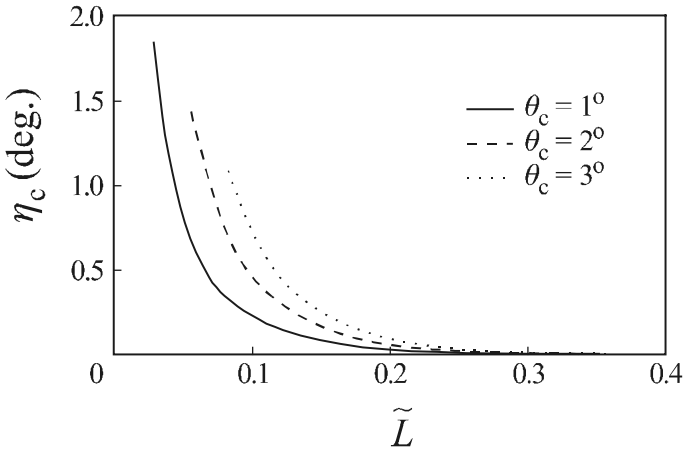

Fig. 9.7. Plot of the inclination angle of contact line, η_c, vs. the dimensionless interparticle distance $\widetilde{L}$ calculated in Ref. [21] for three different values of the angle θ_c determining the size of a 'cork-shaped' particle (Fig. 9.4a); the values of the parameters $qR_0 = 5$ and $\psi_c = 5°$ are fixed.

The dependence of the contact line inclination η_c on the dimensionless interparticle separation $\widetilde{L}$ is illustrated in Fig. 9.7 for three different values of θ_c for *cork-shaped* particles (Fig. 9.4a). The values of the other parameters, $qR_0 = 5$ and $\psi_c = 5°$, are the same for the three curves in Fig. 9.7. For two diametrically opposed particles the inclination disappears because of the symmetry of the system, that is $\eta_c = 0$ for $\widetilde{L} = 1$, see Fig. 9.7. As seen in the figure η_c is small even for short separations $\widetilde{L}$. This fact will be utilized in Section 9.3.3 below in the procedure for calculating the lateral capillary force experienced by *spherical* particles.

9.3. CALCULATION OF THE LATERAL CAPILLARY FORCE

In Fig. 9.4 the particles are pressed against the solid substrate by the meniscus surface tension; the resultant of the force applied on each particle along the normal to the substrate is counterbalanced by the bearing reaction. Our aim below is to calculate the tangential component of the capillary force F_t, which represents the lateral capillary force acting between the two particles. Let $\mathbf{e}_a$ be the unit vector of the particle axis. We denote by $\mathbf{e}_t$ a vector, which is perpendicular to $\mathbf{e}_a$ and belongs to the plane xz, see Fig. 9.4a. Then in view of Eqs. (7.21)–(7.23) the contributions of surface tension and pressure to the lateral capillary force are

$$F_t^{(\sigma)} \equiv \mathbf{e}_t \cdot \oint_C dl \mathbf{m}\sigma, \qquad F_t^{(p)} \equiv \mathbf{e}_t \cdot \oint_S ds(-\mathbf{n}P), \tag{9.40}$$

$$F_t = F_t^{(\sigma)} + F_t^{(p)} \tag{9.41}$$

The integration in Eq. (9.40) is carried out along the three-phase contact line C and throughout the particle surface S. As usual, **n** is the running outer unit normal to the particle surface and **m** is the unit vector in the direction of the surface tension, see Fig. 9.4a; **m** is simultaneously perpendicular to the contact line and tangential to the liquid interface. Following Ref. [21] below we calculate F_t for the cases of fixed contact line and contact angle separately.

9.3.1. BOUNDARY CONDITION OF FIXED CONTACT LINE

This boundary condition reads (see Fig. 9.4):

$$\zeta = h_c = \text{const.} \qquad \text{(at the contact line)} \tag{9.42}$$

In such a case the contact line is a circumference, which is perpendicular to the vector $\mathbf{e}_a$, i.e. to the particle axis. Then the symmetry of the system implies $F_t^{(p)} = 0$. On the other hand, $F_t^{(\sigma)}$ is not zero insofar as the meniscus slope

$$\tan\psi = \frac{1}{\chi}\left(\frac{\partial\zeta}{\partial\tau}\right)_{\tau=\tau_c} \tag{9.43}$$

varies along the contact line (this is a manifestation of contact angle hysteresis); χ is given by Eq. (9.23). The unit vectors of the biconical coordinates, $\mathbf{e}_\omega$, $\mathbf{e}_\tau$ and $\mathbf{e}_r$ (see Fig. 9.5a), form a local basis in each point of the contact line. Then the unit vector in the direction of surface tension can be expressed in the form

$$\mathbf{m} = -\,\mathbf{e}_\tau \cos\psi - \mathbf{e}_r \sin\psi \tag{9.44}$$

Next, we introduce polar coordinates (ρ,ϕ), with running unit vectors $\mathbf{e}_\rho$ and $\mathbf{e}_\phi$, in the plane of the contact line. Then for the points of the contact line one can write

$$\mathbf{e}_\tau = -\,\mathbf{e}_\rho \cos\theta_c + \mathbf{e}_a \sin\theta_c\,, \qquad \mathbf{e}_r = \mathbf{e}_\rho \sin\theta_c + \mathbf{e}_a \cos\theta_c\,. \tag{9.45}$$

Taking into account that $\mathbf{e}_t \cdot \mathbf{e}_\rho = \cos\phi$ and $\mathbf{e}_t \cdot \mathbf{e}_a = 0$ we combine Eqs. (9.44) and (9.45) to obtain

$$\mathbf{e}_t \cdot \mathbf{m} = (\cos\theta_c \cos\psi - \sin\theta_c \sin\psi)\cos\phi \tag{9.46}$$

The assumption for small meniscus slope, Eq. (9.4), used by us implies that angle ψ is small; then in view of Eq. (9.43) we can write

$$\sin\psi \approx \frac{1}{\chi}\left(\frac{\partial\zeta}{\partial\tau}\right)_{\tau=\tau_c} \qquad \cos\psi \approx 1 - \frac{1}{2}\left(\frac{1}{\chi}\frac{\partial\zeta}{\partial\tau}\right)^2_{\tau=\tau_c} \tag{9.47}$$

Recalling that $F_t^{(p)} = 0$, from Eqs. (9.40), (9.46) and (9.47) one obtains

$$F_t = -\sigma_0 r_c \int_0^{\pi} d\phi \cos\phi \left[\frac{1}{\chi^2}\left(\frac{\partial\zeta}{\partial\tau}\right)^2 \cos\theta_c + \frac{2}{\chi}\frac{\partial\zeta}{\partial\tau}\sin\theta_c\right]_{\tau=\tau_c} \tag{9.48}$$

where r_c is given by Eq. (9.39) and higher order terms are neglected. The running angles ϕ and ω provide two alternative parametrizations of the contact line, connected as follows [21]:

$$\cos\phi = \frac{\lambda\cosh\tau_c\cos\omega - 1}{\lambda\cosh\tau_c - \cos\omega}, \qquad \frac{d\phi}{d\omega} = \frac{(\lambda^2\cosh^2\tau_c - 1)^{1/2}}{\lambda\cosh\tau_c - \cos\omega} \tag{9.49}$$

A substitution of Eq. (9.49) into (9.48), in view of Eqs. (9.20) and (9.23), finally yields [21]:

$$F_t = -\sigma_0 R_0 \int_0^{\pi} d\omega(\lambda\cosh\tau_c\cos\omega - 1)\left[\frac{1}{(\lambda^2-1)^{1/2}}\left(\frac{\partial\tilde{\zeta}}{\partial\tau}\right)^2 + \frac{2\sin\theta_c}{\lambda\cosh\tau_c - \cos\omega}\frac{\partial\tilde{\zeta}}{\partial\tau}\right]_{\tau=\tau_c} \tag{9.50}$$

Having solved numerically the boundary problem in the case of fixed contact *line*, see Eqs. (9.34)–(9.36), one can further substitute the result for the computed function $\tilde{\zeta}(\omega,\tau)$ into Eq. (9.50) to calculate the lateral capillary force by means of numerical integration. Results are shown in Section 9.3.4 below.

9.3.2. BOUNDARY CONDITION OF FIXED CONTACT ANGLE

The main difference with the previous Section 9.3.1 is that the contact line in general does not lie in a plane perpendicular to the particle axis, see Fig. 9.8. As a result $F_t^{(p)}$ is no longer zero and the interfacial tension σ can vary along the contact line in accordance with Eq. (9.8). Thus from Eqs. (9.8) and (9.40) one obtains [21]

$$F_t^{(\sigma)} \equiv \oint_C dl(\mathbf{e}_t \cdot \mathbf{m})(\sigma_0 - \Pi_0\zeta_c + ...) \tag{9.51}$$

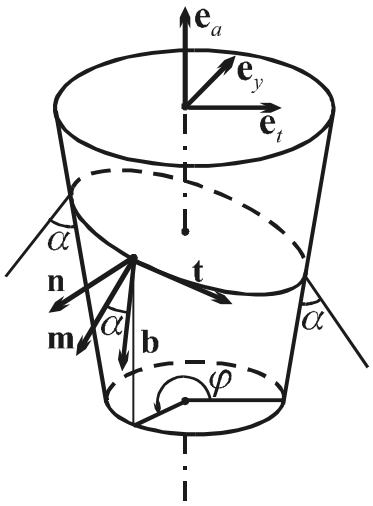

Fig. 9.8. The right-hand-side cork-shaped particle in Fig. 9.4a sketched in an enlarged scale: **t** is a unit vector tangential to the three-phase contact line; **n** is an outer unit normal to the particle surface; $\mathbf{b} = \mathbf{t} \times \mathbf{n}$ is a binormal; **m** is the unit vector in the direction of the surface tension, which is tangential to the liquid meniscus and normal to the contact line; α is the three-phase contact angle.

where ζ_c is defined by Eq. (9.38). First we derive expressions for calculating F_t in the case of cork-shaped particles; the case of spherical particles is considered in Section 9.3.3 below.

The unit vector in direction of the surface tension at the contact line is

$$\mathbf{m} = \mathbf{n}\cos\psi_c + \mathbf{b}\sin\psi_c\,, \qquad \mathbf{b} \equiv \mathbf{t} \times \mathbf{n}\,, \tag{9.52}$$

where, as usual, **n** is the outer unit normal to the particle surface, **t** is the running unit tangent to the contact line; **b** is a binormal and $\psi_c = \pi/2 - \alpha = \text{const.}$, see Fig. 9.8. The unit vectors $\mathbf{e}_t$, $\mathbf{e}_y$ and $\mathbf{e}_a$ form a basis, which can be used to express **n**:

$$\mathbf{n} = \mathbf{e}_t\cos\theta_c\cos\phi + \mathbf{e}_y\cos\theta_c\sin\phi - \mathbf{e}_a\sin\theta_c \tag{9.53}$$

Let us denote by **R** the running position vector of a point from the contact line; then

$$\mathbf{t} = \frac{1}{t_c}\frac{\partial \mathbf{R}}{\partial\phi}, \qquad \mathbf{R} \equiv [R_0 + \zeta_c(\phi)]\mathbf{e}_r \tag{9.54}$$

where

$$t_c^2 \equiv (R_0 + \zeta_c)^2\sin^2\theta_c + (\mathrm{d}\zeta_c/\mathrm{d}\phi)^2, \quad \mathbf{e}_r = \mathbf{e}_t\sin\theta_c\cos\phi + \mathbf{e}_y\sin\theta_c\sin\phi + \mathbf{e}_a\cos\theta_c \tag{9.55}$$

By means of Eqs. (9.52)–(9.55) one can prove that

$$\mathbf{e}_t \cdot \mathbf{m} = -\left[\frac{d\zeta_c}{d\phi}\cos^2\theta_c\sin\phi + \frac{d(|R|\sin\phi)}{d\phi}\sin^2\theta_c\right]\frac{\sin\psi_c}{t_c} + \cos\theta_c\cos\psi_c\cos\phi \tag{9.56}$$

Further we substitute Eq. (9.56) into Eq. (9.51) to obtain [21]:

$$F_t^{(\sigma)} = -2\sigma_0 \cos\theta_c (\cos\theta_c \sin\psi_c + \sin\theta_c) \int_0^{\pi} d\phi \frac{d\zeta_c}{d\phi} \sin\phi + \cos\theta_c \int_0^{\pi} d\phi \cos\phi \left[\frac{\sigma_0}{r_0} \left(\frac{d\zeta_c}{d\phi} \right)^2 - 2\Pi_0 r_0 \zeta_c \right] \tag{9.57}$$

where higher-order terms have been neglected. To calculate $F_t^{(p)}$ we integrate the pressure throughout the lateral surface of the cork-shaped particle (Fig. 9.8); thus using Eqs. (9.40) and (9.53) we get

$$F_t^{(p)} = -\cos\theta_c \int_0^{2\pi} d\phi \sin\theta_c \cos\phi \left(P_R \int_{r_1}^{R_0+\zeta_c} r dr + P_{\mathrm{II}} \int_{R_0+\zeta_c}^{r_2} r dr \right) \tag{9.58}$$

where r_1 and r_2 are boundaries of integration satisfying the relationship $r_1 \le \zeta_c(\phi) \le r_2$ for any ϕ; the exact choice of r_1 and r_2 is not important, because they drop out from the final expression for $F_t^{(p)}$. Indeed, integrating in Eq. (9.58), substituting P_R from Eq. (9.18), and neglecting higher order terms one obtains [21]:

$$F_t^{(p)} = 2(\Pi_0 - 2\sigma_0/R_0) r_0 \cos\theta_c \int_0^{\pi} d\phi \, \zeta_c \cos\phi \tag{9.59}$$

Next, we integrate by parts in Eq. (9.59), and combine the result with Eqs. (9.41) and (9.57):

$$F_t = -2\sigma_0 \cos\theta_c (\cos\theta_c \sin\psi_c - \sin\theta_c) \int_0^{\pi} d\phi \frac{d\zeta_c}{d\phi} \sin\phi + \frac{\sigma_0}{r_0} \cos\theta_c \int_0^{\pi} d\phi \left(\frac{d\zeta_c}{d\phi} \right)^2 \cos\phi \tag{9.60}$$

Note that the terms with Π_0 in Eqs. (9.57) and (9.59) cancel each other. The numerical procedure from Section 9.2.4 gives $\tilde{\zeta}(\omega, \tau)$; therefore it is more convenient to rearrange Eq. (9.60) using ω instead of ϕ as integration variable; by means of Eqs. (9.20) and (9.49) one obtains [21]:

$$\tilde{F}_t = -2 (\cos\theta_c \sin\psi_c - \sin\theta_c) \int_0^{\pi} d\omega \frac{d\tilde{\zeta}_c}{d\omega} \frac{\sin\omega \cot\theta_a \sqrt{\lambda^2 - 1}}{\lambda \cosh\tau_c - \cos\omega} + \frac{\cos\theta_c}{\sqrt{\lambda^2 - 1}} \int_0^{\pi} d\omega \left(\frac{d\tilde{\zeta}_c}{d\omega} \right)^2 (\lambda \cosh\tau_c \cos\omega - 1) \tag{9.61}$$

where $\widetilde{\zeta}_c \equiv \widetilde{\zeta}(\omega, \tau_c)$ and $\widetilde{F}_t$ denotes the dimensionless lateral capillary force:

$$\widetilde{F}_t \equiv F_t / (\sigma_0 R_0) \tag{9.62}$$

To calculate the capillary force F_t one has to first determine $\widetilde{\zeta}(\omega, \tau)$ solving numerically Eq. (9.24) and then to use Eq. (9.50) or (9.61) depending on whether the case of fixed contact *line* or *angle*, respectively, is considered.

Note that in the case of fixed contact *angle* Eq. (9.61) contains the derivative $\partial\widetilde{\zeta} / \partial\omega$ and consequently the capillary force F_t stems from the inclination of the contact line. In contrast, when the contact *line* is fixed at the particle surface, Eq. (9.50) contains only the derivative $\partial\widetilde{\zeta} / \partial\tau$ and then F_t originates from the variation of meniscus slope along the contact line.

9.3.3. CALCULATION PROCEDURE FOR CAPILLARY FORCE BETWEEN SPHERICAL PARTICLES

As already mentioned, if the boundary condition for fixed contact *line*, Eq. (9.42) is used, then the capillary force F_t is calculated from Eq. (9.50) in the same way for spherical particles (Fig. 9.4b) and cork-shaped particles (Fig. 9.4a). Indeed, in both cases the contact line is an immobile circumference perpendicular to the particle-substrate axis. In other words, if the contact line is fixed, then F_t is identical for spherical and cork-shaped particles having the same radius of the contact line.

In contrast, if the boundary condition for fixed contact angle, Eq. (9.29), is imposed, then the contact line moves along the particle surface when the interparticle separation L varies. In addition, when the two particles approach each other (i) the capillary elevation of the contact line h_c defined by Eq. (9.37) increases (Fig. 9.6), and (ii) the inclination angle η_c defined by Eq. (9.39) also increases. As demonstrated in Fig. 9.7 for not too small values of the separation L the inclination angle is rather small ($\tan\eta_c << 1$) and the contact line is almost perpendicular to the particle-substrate axis. This fact allows one to utilize the following approximate two-step procedure, which is analogous to that used in Section 7.3.2 for the case of a planar interface.

At the *first* step, as a zeroth approximation one assumes that the contact line lies in a plane perpendicular to the axis determined by angle θ_a (Fig. 9.4b). In such a case the contact line is a circumference of radius r_c elevated at a distance h_c from the reference sphere of radius R_0.

At the *second* step one formally replaces the sphere by a cork shaped particle having the same values of θ_c, ψ_c and h_c, as well as of r_c , θ_a , τ_c , etc. Next, one solves numerically Eq. (9.24), along with the boundary conditions (9.29) and (9.33) and substitutes the result for $\tilde{\zeta}(\omega,\tau)$ in Eq. (9.61) to calculate the capillary force F_t. The value of F_t thus obtained, which is accurate for the cork-shaped particle, gives a first approximation for the capillary force exerted on the spherical particle.

Note that for different values of the distance L between two spherical particles the contact radius r_c and the capillary elevation h_c (Fig. 9.6) are different, and consequently, using the above procedure we replace the sphere with different cork-shaped particles (with different θ_c). This reflects the shrinking of the contact line on the spherical surface with the increase of h_c.

The mathematical background of the above procedure is the following [21]. The radius of the contact line r_c can be related to the radius of the reference sphere R_0 and the particle radius R_p (Fig. 9.4b):

$$r_c = R_0 (1 + \bar{h}_c \sin\psi_c)\sin\theta_c = R_p \sin(\alpha + \theta_c + \psi_c) , \tag{9.63}$$

We have introduced the notation $\bar{h}_c \equiv h_c/(R_0 \sin\psi_c)$; for the numerical calculations it is important that $\bar{h}_c$ is insensitive to the value of ψ_c. The length of the segment OM in Fig. 9.4b can be expressed in a similar way:

$$|\mathrm{OM}| = R_0 (1 + \bar{h}_c \sin\psi_c)\cos\theta_c = R_0 - h_0 + R_p [1 + \cos(\alpha + \theta_c + \psi_c)] , \tag{9.64}$$

The angle $\beta \equiv \alpha + \theta_c + \psi_c$ is also shown in Fig. 9.4b. From Eqs. (9.63) and (9.64) one eliminates angle β and obtains:

$$\psi_c(\theta_c) = \arcsin ((Y - 1)/\bar{h}_c) , \tag{9.65}$$

where

$$Y \equiv (1 - h_0/R_0 + R_p/R_0)\cos\theta_c + [(R_p/R_0)^2 - (1 - h_0/R_0 + R_p/R_0)^2 \sin^2\theta_c]^{1/2} \tag{9.66}$$

Now we can formulate a procedure of calculations, which is based on the above equations [21]:

The input parameters are R_p/R_0, h_0/R_0, qR_0, α and θ_a.

Further, θ_c and ψ_c are calculated as follows.

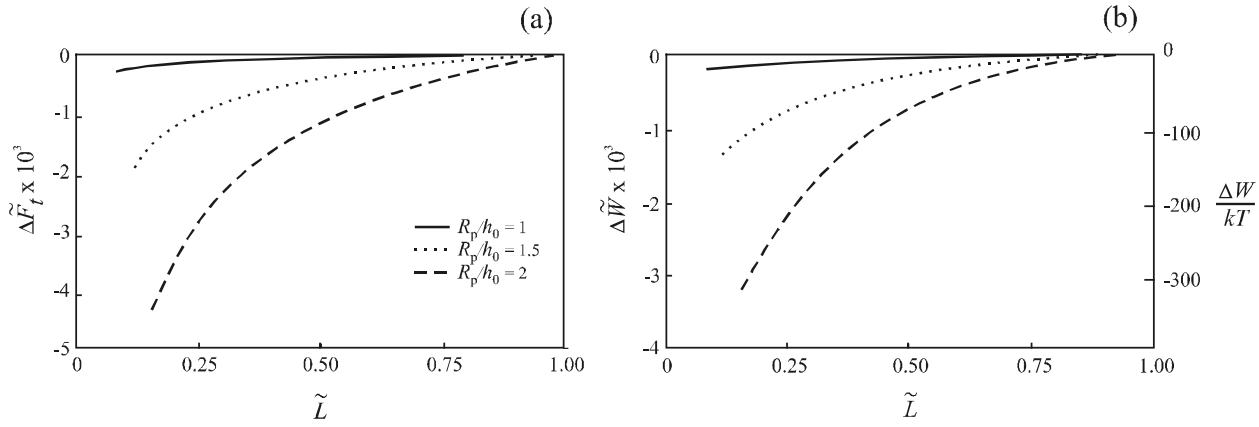

Fig. 9.9. Dimensionless (a) force $\tilde{F}_t$ and (b) energy $\Delta\tilde{W}$ of capillary interaction plotted against the dimensionless separation $\tilde{L}$ between two spherical particles entrapped in a spherical liquid film (Fig. 9.4b). The three different curves, calculated in Ref. [21], correspond to three values of the parameter R_p/h_0; the values of the other parameters are fixed: $qR_0 = 1$ and $\alpha = 60°$. The right-hand-side scale of $\Delta W/kT$ shows the value of the capillary interaction energy for the special case of $R_0 = 1$ μm, $T = 298$ K and $\sigma_0 = 30$ mN/m.

(i) One chooses an initial guess for θ_c and ψ_c.

(ii) $\tilde{\zeta}(\omega,\tau)$ is obtained by numerical integration of Eq. (9.24), along with the boundary conditions (9.29) and (9.33), as described in Section 9.2.4.

(iii) Next, $\bar{h}_c = \tilde{h}_c/\sin\psi_c$ is determined by numerical calculation of the integral in Eq. (9.37).

(iv) A new value of ψ_c is calculated from Eqs. (9.65)–(9.66).

(v) A new value of θ_c is obtained by solving numerically Eq. (9.63).

The next iteration repeats from point (ii) with the new values of ψ_c and θ_c until convergence is achieved.

(vi) With the obtained final parameter values and $\tilde{\zeta}(\omega,\tau)$ one calculates the dimensionless capillary force $\tilde{F}_t$ from Eq. (9.61) for various θ_a, that is for various values of the dimensionless interparticle separation $\tilde{L} = 2\theta_a/\pi$; $\tilde{F}_t$ thus calculated corresponds to the boundary condition of fixed contact *angle*.

(vii) If the boundary condition for fixed contact *line* is used, then h_c and θ_c are input parameters (instead of α and R_p/R_0) and steps (i)–(vi) are not necessary. In this case Eq. (9.24) is integrated

numerically using the boundary conditions (9.33)–(9.36); next, the capillary force is calculated from Eq. (9.50).

(viii) Finally, one can determine the energy of lateral capillary interaction ΔW by integration:

$$\Delta\widetilde{W}(\widetilde{L}) \equiv \frac{\Delta W(\widetilde{L})}{\sigma_0 R_0^2} = \pi \int_{\widetilde{L}}^{1} \widetilde{F}_t(\widetilde{L})\, d\widetilde{L} \tag{9.67}$$

where $\Delta\widetilde{W}$ is the dimensionless interaction energy. The additive constant in the energy is determined in such a way, that $\Delta W = 0$ for two diametrically opposed particles, i.e. for $\widetilde{L} = 1$.

9.3.4. NUMERICAL RESULTS FOR THE FORCE AND ENERGY OF CAPILLARY INTERACTION

Using the procedure described in Section 9.3.3 the force and energy of capillary interaction between two spherical particles entrapped into a spherical liquid film (Fig. 9.4b) have been calculated [21]. Results for the case of fixed contact angle ($\alpha = 60°$) are shown in Figs. 9.9a and 9.9b, where the dimensionless force and energy, $\widetilde{F}_t$ and $\Delta\widetilde{W}$ [see Eqs. (9.62) and (9.67)], are plotted against the dimensionless interparticle separation $\widetilde{L} = L/(\pi R_0)$; the range of variation of $\widetilde{L}$ is $2\theta_c/\pi < \widetilde{L} \leq 1$. The negative values of $\widetilde{F}_t$ and $\Delta\widetilde{W}$ mean that the interaction is attractive. The three curves are calculated for three different values of the ratio R_p/h_0 corresponding to different magnitude of the particle protrusion from the film surface. As could be expected, the larger the protrusion (the larger the deformation), the stronger the capillary attraction. To determine ΔW from $\Delta\widetilde{W}$ one is to specify the values of σ_0 and R_0. The right-hand-side scale of $\Delta W/kT$ (Fig. 9.9b) shows the capillary interaction energy for a special choice of the parameters: $R_0 = 1$ μm, $T = 298$ K and $\sigma_0 = 30$ mN/m. Note that ΔW is of the order of (100–300)kT despite of the small size of the particles ($R_p = 50$ nm). Such a strong attraction is typical for the capillary force of immersion type, see Fig. 8.3.

Figures 9.10 and 9.11 illustrate the effect of θ_c: the dimensionless interaction energy, $\Delta\widetilde{W} = \Delta W/(\sigma_0 R_0{}^2)$, is plotted against the dimensionless distance, $\widetilde{L}$. At a given R_0, the size of the particles is determined by the angle θ_c, which for the curves in Figs. 9.10 and 9.11 takes

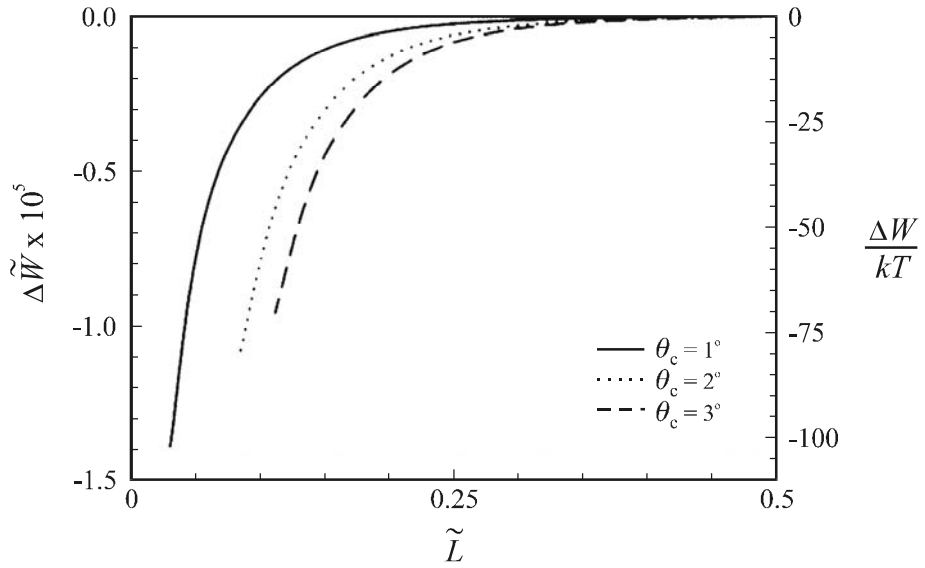

Fig. 9.10. Case of fixed contact angle: dimensionless energy $\Delta\tilde{W}$ of capillary interaction plotted against the dimensionless separation $\tilde{L}$ between two cork-shaped particles entrapped in a spherical liquid film (Fig. 9.4a). The three curves, calculated in Ref. [21], correspond to three values of θ_c denoted in the figure; the other parameters are $\psi_c = 5°$ and $qR_0 = 5$. The right-hand-side scale of $\Delta W/kT$ is as in Fig. 9.9.

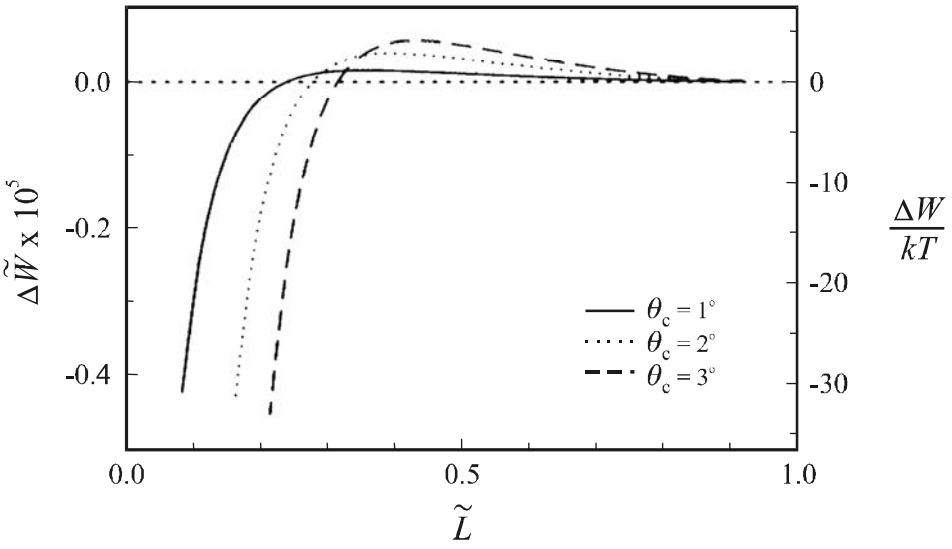

Fig. 9.11. Case of fixed contact line: dimensionless energy $\Delta\tilde{W}$ of capillary interaction vs. dimensionless separation $\tilde{L}$ between two cork-shaped particles entrapped in a spherical liquid film (Fig. 9.4a). The three curves are calculated in Ref. [21] with the same values of θ_c as in Fig. 9.10; for each curve h_c/R_0 is fixed and equal to the respective values of h_∞/R_0 (0.00389, 0.00585 and 0.00719) for the curves in Fig. 9.10. The right-hand-side scale of $\Delta W/kT$ is as in Fig. 9.9.

values 1°, 2° and 3°, i.e. the particles are small, $r_c << R_0$. One sees again that the dimensional interaction energy ΔW can be of the order of (10−100)kT. From a physical viewpoint $\Delta W/kT >> 1$ means that the capillary attraction prevails over the thermal motion and can bring about particle aggregation and ordering in the spherical film.

Note that the parameters values in Figs. 9.10 and 9.11 are chosen in such a way, that the shape of the fluid interfaces to be identical in the state of zero energy, i.e. for two diametrically opposed particles. This provides a basis for quantitative comparison of the plots of ΔW vs. $\tilde{L}$ in these two figures, calculated by using the two alternative boundary conditions. The curves in Fig. 9.10 (as well as in Fig. 9.9) are calculated assuming fixed contact *angle*; one sees that the interaction energy ΔW is always negative, i.e. corresponds to attraction. On the other hand, the curves in Fig. 9.11 are calculated assuming fixed contact *line*. In the latter case the interaction energy changes its sign at comparatively large interparticle distances: attractive at short distances becomes repulsive at large separations.

The fact that that the interaction energy can change sign in the case of fixed contact *line*, but the energy is always negative in the case of fixed contact *angle*, is discussed in Ref. [21]. It is concluded that the non-monotonic behavior of the capillary interaction energy (Fig. 9.11) is a non-trivial effect stemming from the *spherical* geometry of the film coupled with the boundary condition of fixed contact line; such an effect is difficult to anticipate by physical insight. Note that in the case of *planar* geometry the capillary force between identical particles is always monotonic attraction.

9.4. SUMMARY

The fluid interfaces acquire spherical shape when the gravitational deformations are negligible. Hence, lateral capillary forces of “flotation” type (Chapter 8), which are due to the particle weight, do not appear between particles attached to a *spherical* interface, liquid film or membrane. The capillary forces in this case can be only of “immersion” type (Chapter 7). In such a case the origin of the interfacial deformation and the capillary force is the entrapment of particles in the membrane of a spherical multilayered liposome (Fig. 9.1b), as well as in “opened” (Fig. 9.2) and “closed” (Fig. 9.4) liquid films. Interfacial (membrane) deformations

and lateral capillary interactions can originate also from stresses due to outer bodies, like the microfilament in Fig. 9.3a and the microtubule in Fig. 9.3b.

The calculation of the capillary force between particles trapped in spherical films is affected by the specificity of the spherical geometry. For example, the condition for constancy of the volume of the liquid in a closed spherical film (Fig. 9.4) leads to a connection between the particle "capillary charge" Q and the pressure P_R within the film, see Eq. (9.18). The stability of such a film is provided by the repulsive disjoining pressure Π exerted on its surfaces. The disjoining pressure effect determines the capillary length q^{-1}, see Eq. (9.11), and consequently, the range of the lateral capillary forces. If disjoining pressure is missing (as it is in Fig. 9.3) then q is an imaginary number and the Laplace equation, Eq. (9.19), has oscillatory solutions. In our numerical solutions we have assumed that the effect of disjoining pressure is predominant (this guarantees the stability of the films in Figs. 9.2 or 9.4), and we work with real values of the parameter q.

The spherical bipolar coordinates, Eq. (9.21), represent the natural set of coordinates for the mathematical description of the considered system: two axisymmetric particles entrapped into a spherical liquid film. Thus the integration domain is reduced to a rectangle (Fig. 9.5) and the numerical solution of the Laplace equation is made easier. The two types of boundary conditions, fixed contact angle, Eq. (9.29), or fixed contact line, Eq. (9.31), lead to two different expressions for the lateral capillary force, Eqs. (9.61) and (9.50), respectively. The calculation of the capillary interaction between two spherical particles is more complicated in the case of fixed contact *angle* due to the mobility of the contact line; to solve the problem in Section 9.3.3 we have employed auxiliary cork-shaped particles. The interaction energy is always negative (attractive) in the case of fixed contact *angle* (Figs. 9.9 and 9.10). On the other hand, it turns out that the energy can change sign in the case of fixed contact *line* (attractive at short distances but repulsive at long distances, Fig. 9.11). This non-monotonic behavior of the capillary interaction energy is a non-trivial effect stemming from the specificity of the *spherical* geometry coupled with the boundary condition of fixed contact line; such an effect does not exist in the case of *planar* geometry, for which the capillary force between identical particles is always monotonic attraction.

The magnitude of the capillary interaction energy can be of the order of 10−100 kT, see Figs. 9.9 – 9.11, for sub-micrometer (Brownian) particles. In such a case, the capillary attraction prevails over the thermal motion and can bring about particle aggregation and ordering in the spherical film. In this respect, the physical situation is the same for spherical and planar films, if only the particles are subjected to the action of the lateral immersion force.

9.5. REFERENCES

1. J. Sjöblom (Ed.), Emulsions and Emulsion Stability, M. Dekker, New York, 1996.
2. S. Hyde, S. Anderson, K. Larsson, Z. Blum, T. Landh, S. Lidin, B.W. Ninham, The Language of Shape, Elsevier, Amsterdam, 1997.
3. A.G. Volkov, D.W. Deamer, D.L. Tanelian, V.S. Markin, Liquid Interfaces in Chemistry and Biology, Wiley, New York, 1998.
4. S. Hartland, Coalescence in Dense-Packed Dispersions, in: I.B. Ivanov (Ed.) Thin Liquid Films, M. Dekker, New York, 1988; p. 663.
5. H. Wangqi, K.D. Papadopoulos, Colloids Surf. A 125 (1997) 181.
6. S.U. Pickering, J. Chem. Soc. 91 (1907) 2001.
7. Th. F. Tadros, B. Vincent, in: P. Becher (Ed.) Encyclopedia of Emulsion Technology, Vol. 1, Marcel Dekker, New York, 1983, p. 129.
8. N.D. Denkov, I.B. Ivanov, P.A. Kralchevsky, J. Colloid Interface Sci. 150 (1992) 589.
9. N. Yan, J.H. Masliyah, Colloids Surf. A 96 (1995) 229 and 243.
10. B.R. Midmore, Colloids Surf. A 132 (1998) 257.
11. H.M. Princen, The Equilibrium Shape of Interfaces, Drops, and Bubbles, in: E. Matijevic, (Ed.) Surface and Colloid Science, Vol. 2, Wiley, New York, 1969, p. 1.
12. C. Dietrich, M. Angelova, B. Pouligny, J. Phys. II France 7 (1997) 1651.
13. K. Velikov, C. Dietrich, A. Hadjiisky, K.D. Danov, B. Pouligny, Europhys. Lett. 40, (1997) 405.
14. K. Velikov, K.D. Danov, M. Angelova, C. Dietrich, B. Pouligny, Colloids Surf. A, 149 (1998) 245.

15. K.D. Danov, B. Pouligny, M.I. Angelova, P.A. Kralchevsky, "Strong Capillary Attraction between Spherical Inclusions in a Multilayered Lipid Membrane", in: Studies in Surface Science and Catalysis, Vol. 132, Elsevier, Amsterdam, 2001; pp. 519-524. See also K. D. Danov, B. Pouligny, P. A. Kralchevsky, "Capillary forces between colloidal particles confined in a liquid film: the finite-meniscus problem", Langmuir 17 (2001) 6599-6609.

16. D.E. Ingber, Ann. Rev. Physiol. 59 (1997) 575.

17. D.E. Ingber, Scientific American, January 1998, p. 30.

18. J.N. Israelachvili, Biochim. Biophys. Acta 469 (1977) 221.

19. A.G. Petrov, I. Bivas, Prog. Surface Sci. 16 (1984) 389.

20. P.A. Kralchevsky, V.N. Paunov, N.D. Denkov, K. Nagayama, J. Chem. Soc. Faraday Trans. 91 (1995) 3415.

21. P.A. Kralchevsky, V.N. Paunov, K. Nagayama, J. Fluid. Mech. 299 (1995) 105.

22. L.D. Landau, E.M. Lifshitz, Fluid Mechanics, Pergamon Press, Oxford, 1984.

23. P.A. Kralchevsky, I.B. Ivanov, J. Colloid Interface Sci. 137 (1990) 234.

24. I.B. Ivanov, P.A. Kralchevsky, Mechanics and thermodynamics of curved thin films, in: I.B. Ivanov (Ed.) Thin Liquid Films, M. Dekker, New York, 1988; p. 49.

25. I.B. Ivanov, B.V. Toshev, Colloid Polymer Sci. 253 (1975) 593.

26. B.V. Derjaguin, N.V. Churaev, V.M. Muller, V.M., Surface Forces, Plenum Press: Consultants Bureau, New York, 1987.

27. C.E. Weatherburn, Differential Geometry of Three Dimensions, Cambridge University Press, Cambridge, 1939.

28. L. Brand, Vector and Tensor Analysis, Wiley, 1947.

29. A.J. McConnell, Application of Tensor Analysis, Dover, New York, 1957.

30. G.A. Korn, T.M. Korn, Mathematical Handbook, McGraw-Hill, New York, 1968.

31. A. Constantinides, Applied Numerical Methods with Personal Computers, McGraw-Hill, New York, 1987.

32. R.W. Hockney, J.W. Eastwood, Computer Simulation Using Particles, McGraw-Hill, New York, 1981.